High-Order FVTD on Unstructured Grids

Dmitry Firsov[1], Joe LoVetri[1], Ian Jeffrey[1], Vladimir Okhmatovski[1], Walid Chamma[2]

[1]Department of Electrical and Computer Engineering
University of Manitoba, Winnipeg, MB, Canada, R3T 5V6
firsovd@ee.umanitoba.ca, lovetri@ee.umanitoba.ca

[2]Radar Electronic Warfare Section
Defence R&D Canada - Ottawa, Department of National Defence
3701 Carling Avenue, Ottawa, Ontario, K1A 0Z4
Walid.Chamma@drdc-rddc.gc.ca

Abstract: Computational results obtained using a Finite-Volume Time-Domain (FVTD) engine for solving Maxwell's Equations on unstructured grids are presented. The FVTD engine uses the MUSCL and polynomial interpolation methods to approximate the fluxes at the cell boundaries up to a third order of accuracy. Results are presented for the transient scattering from a PEC sphere and almost perfect agreement with the analytic solution in the time-domain is achieved. The number of cells required as compared to FDTD is substantial reduced.

Keywords: Finite-Volume Time-Domain, FVTD, Maxwell's Equations.

1. Introduction

The FDTD algorithm is probably the most popular computational electromagnetics (CEM) technique in use today. The two main drawbacks of the *standard* FDTD method is that curved geometries must be approximated by "stair-stepping" the boundaries and that the electromagnetic field components are interlaced in space and time. These drawbacks require that a fine grid be used in order to resolve curved boundaries increasing the computational resources. There have been several successful investigations on modifying the method for non-rectangular boundaries but these are difficult to implement and use [1].

The finite-volume technique is a standard technique used in Computational Fluid Dynamics (CFD) [2]. One of the first comprehensive implementations of the technique for Computational Electromagnetics (CEM) was reported by Shankar *et al*. in the early 1990's [3]. This method collocates all the field components at the centre of each finite volume and is implemented on structured body-fitted curvilinear grids. It is a characteristic-based FVTD scheme which uses a two-step second-order upwinding scheme in the time domain. A similar technique has also been presented by Shang and others [4]. Recently, two other groups have reported on achieving excellent results using a characteristic-based FVTD technique [5, 6]. These use a second order accurate MUSCL scheme to interpolate the fluxes at the finite-volume facets.

In this paper we present the use of a higher-order interpolatory method, developed by Ollivier-Gooch for fluid-dynamics problems [7], for our FVTD Maxwell equation solver. The engine was implemented using object-oriented techniques, the details can be found elsewhere. Here we provide details of the algorithm and show results comparing FDTD, FVTD using the MUSCL interpolation, and FVTD with third-order interpolation, for the problem of the transient scattering from a PEC sphere.

In Section 2 we give a brief overview of the theory behind the FVTD method as it pertains to Maxwell's equations. In Section 3 we discuss schemes for flux integration, namely MUSCL and polynomial interpolation schemes. Finally, in Section 4 we compare computational results to the analytic solution and FDTD for the scattering from a PEC sphere.

2. FVTD for Conservation Laws and Maxwell's Equations

The FVTD algorithm is usually applied to physical phenomena which are governed by a *conservation law*. For example, given a scalar quantity, denoted by $u(x, t)$, a typical conservation law would be

$$\partial_t u(x, t) + \nabla \cdot f(u(x, t)) = S(x, t) \tag{1}$$

where the flux vector f is some function of u, $S(x, t)$ is a source term. Integrating the conservation law over an arbitrary volume, T_i, with boundary ∂T_i gives:

$$\int_{T_i} \partial_t u(x, t) dV + \int_{\partial T_i} f(u(x, t)) \cdot ds = \int_{T_i} S(x, t) dV \tag{2}$$

where the divergence theorem has been applied to the second term and $ds = \hat{n} ds$ is the outward directed surface element vector. The FVTD method for solving electromagnetic problems considers all of the electric and magnetic field components as components of a solution vector: $u = [\ E\ H\ ]^T$, and then casts Maxwell's equations into a form analogous to (1). We now follow a procedure similar to that given in [5]. Starting from Maxwell's two curl equations:

$$\begin{cases} \varepsilon \partial_t E - \nabla \times H + \sigma E = -J \\ \mu \partial_t H + \nabla \times E = 0 \end{cases} \tag{3}$$

we employ the matrix operator

$$S(x)b = \begin{bmatrix} 0 & -x_3 & x_2 \\ x_3 & 0 & -x_1 \\ -x_2 & x_1 & 0 \end{bmatrix} \begin{bmatrix} b_1 \\ b_2 \\ b_3 \end{bmatrix} = x \times b \tag{4}$$

by which the curl of a vector can be expressed in terms of the divergence of a matrix operating on the vector:

$$\nabla \times x \equiv (\text{div} S(x))^T = \begin{bmatrix} \partial_2 x_3 - \partial_3 x_2, & -\partial_1 x_3 + \partial_3 X_1, & \partial_1 x_2 - \partial_2 x_1 \end{bmatrix}^T. \tag{5}$$

In terms of this new operator, Maxwell's equations can be written as

$$\begin{cases} \varepsilon \partial_t E - (\text{div} S(H))^T + \sigma E = -J \\ \mu \partial_t H + (\text{div} S(E))^T = 0 \end{cases} \tag{6}$$

or, even more succinctly as

$$\partial_t u + \alpha^{-1} K u = \alpha^{-1} (G + Bu) \tag{7}$$

where

$$\alpha \triangleq \begin{bmatrix} \varepsilon & \mathbf{0} \\ \mathbf{0} & \mu \end{bmatrix}, \quad \mathbf{Ku} = \begin{bmatrix} -\nabla \times \mathbf{H} \\ \nabla \times \mathbf{E} \end{bmatrix}, \quad \mathbf{B} \triangleq \begin{bmatrix} -\sigma & \mathbf{0} \\ \mathbf{0} & \mathbf{0} \end{bmatrix}, \quad \mathbf{G} \triangleq \begin{bmatrix} -\mathbf{J} \\ \mathbf{0} \end{bmatrix}. \tag{8}$$

Integrating the curl equations (7) over an element denoted by T_i with boundary ∂T_i and using the divergence theorem to convert the integral over volume to integrals over the surface as in we may arrive at

$$\int_{T_i} \partial_t \mathbf{u} \, d\mathbf{x} + \int_{\partial T_i} \alpha^{-1} \mathbf{A}(\hat{\mathbf{n}}) \mathbf{u} \, ds = \int_{T_i} \alpha^{-1} \mathbf{G} \, d\mathbf{x} + \int_{T_i} \alpha^{-1} \mathbf{B} \mathbf{u} \, d\mathbf{x}. \tag{9}$$

where matrix $\mathbf{A}(\hat{\mathbf{n}})$ is defined by

$$\mathbf{A}(\hat{\mathbf{n}}) = \begin{bmatrix} \mathbf{0} & -\mathbf{S}(\hat{\mathbf{n}}) \\ \mathbf{S}(\hat{\mathbf{n}}) & \mathbf{0} \end{bmatrix}. \tag{10}$$

and $\hat{\mathbf{n}}$ denotes the outward normal to the volume surface ∂T_i. Next we define $\tilde{\mathbf{A}}(\hat{\mathbf{n}}) \triangleq \alpha^{-1} \mathbf{A}(\hat{\mathbf{n}})$ and we decompose $\tilde{\mathbf{A}}(\hat{\mathbf{n}})$ as a sum of matrices with positive and negative eigenvalues (due to the symmetry of $\mathbf{A}(\hat{\mathbf{n}})$. the eigenvalues are real). Limiting each volumetric element to a homogeneous isotropic space described by material parameters $\varepsilon = \mathrm{diag}(\varepsilon, \varepsilon, \varepsilon)$ and $\mu = \mathrm{diag}(\mu, \mu, \mu)$ it can be shown that the matrix $\tilde{\mathbf{A}}(\hat{\mathbf{n}})$ has six eigenvalues given by $\Lambda = \mathrm{diag}\{0, 0, v, v, -v, -v\}$ where $v = 1/\sqrt{\varepsilon\mu}$. Further manipulation yields the decomposition of $\tilde{\mathbf{A}}(\hat{\mathbf{n}})$ into

$$\tilde{\mathbf{A}}(\hat{\mathbf{n}}) = \tilde{\mathbf{A}}(\hat{\mathbf{n}})^+ + \tilde{\mathbf{A}}(\hat{\mathbf{n}})^- \tag{11}$$

where it can be shown that

$$\tilde{\mathbf{A}}(\hat{\mathbf{n}})^+ = \frac{1}{2}\begin{bmatrix} v\mathbf{S}(\hat{\mathbf{n}})^2 & -\varepsilon^{-1}\mathbf{S}(\hat{\mathbf{n}}) \\ \mu^{-1}\mathbf{S}(\hat{\mathbf{n}}) & v\mathbf{S}(\hat{\mathbf{n}})^2 \end{bmatrix}, \quad \tilde{\mathbf{A}}(\hat{\mathbf{n}})^- = \frac{1}{2}\begin{bmatrix} -v\mathbf{S}(\hat{\mathbf{n}})^2 & -\varepsilon^{-1}\mathbf{S}(\hat{\mathbf{n}}) \\ \mu^{-1}\mathbf{S}(\hat{\mathbf{n}}) & -v\mathbf{S}(\hat{\mathbf{n}})^2 \end{bmatrix}. \tag{12}$$

We now use $\mathbf{u}^*$ to denote the flux on the inside part of the surface ∂T_i while using $\mathbf{u}^{**}$ to denote the flux on the outside part. We can consider fluxes $\mathbf{u}^*$ and $\mathbf{u}^{**}$ as limits of the solution $\mathbf{u}(\mathbf{x})$ from the inside or outside of the element on to ∂T_i. The electromagnetic boundary conditions for the continuity of the tangential electric and magnetic field components across a boundary,

$$\begin{cases} \hat{\mathbf{n}} \times \mathbf{E}^* = \hat{\mathbf{n}} \times \mathbf{E}^{**} = \hat{\mathbf{n}} \times \mathbf{E} \\ \hat{\mathbf{n}} \times \mathbf{H}^* = \hat{\mathbf{n}} \times \mathbf{H}^{**} = \hat{\mathbf{n}} \times \mathbf{H} \end{cases}, \tag{13}$$

can be expressed in terms of the operator $\mathbf{A}(\hat{\mathbf{n}})$ as $\mathbf{A}(\hat{\mathbf{n}})\mathbf{u}^* = \mathbf{A}(\hat{\mathbf{n}})\mathbf{u}^{**}$. What is needed at the surface of an element is the vector $\mathbf{A}(\hat{\mathbf{n}})\mathbf{u}$ which, because of the boundary conditions, is $\mathbf{A}(\hat{\mathbf{n}})\mathbf{u} = \mathbf{A}(\hat{\mathbf{n}})\mathbf{u}^* = \mathbf{A}(\hat{\mathbf{n}})\mathbf{u}^{**}$. But $\mathbf{u}^*$ and $\mathbf{u}^{**}$ are not known and must be interpolated from the known values in the cell interior. This is accomplished by first calculating $\hat{\mathbf{n}} \times \mathbf{E}$ and $\hat{\mathbf{n}} \times \mathbf{H}$ at the cell boundary. Let us consider the top and bottom blocks of $\tilde{\mathbf{A}}(\hat{\mathbf{n}})^+ \mathbf{u}^*$ and $\tilde{\mathbf{A}}(\hat{\mathbf{n}})^- \mathbf{u}^{**}$ separately. The top block is

$$\frac{1}{2}v_1 \mathbf{S}(\hat{\mathbf{n}})^2 \mathbf{E}^* - \frac{1}{2}\frac{\mathbf{S}(\hat{\mathbf{n}})}{\varepsilon_1}\mathbf{H}^* \quad \text{and} \quad -\frac{1}{2}v_2 \mathbf{S}(\hat{\mathbf{n}})^2 \mathbf{E}^{**} - \frac{1}{2}\frac{\mathbf{S}(\hat{\mathbf{n}})}{\varepsilon_2}\mathbf{H}^{**} \tag{14}$$

We multiply the first by ε_1 and the second by ε_2 to get

$$\frac{1}{2}Y_1 S(\hat{n})^2 E^* - \frac{1}{2}S(\hat{n})H^* \text{ and } -\frac{1}{2}Y_2 S(\hat{n})^2 E^{**} - \frac{1}{2}S(\hat{n})H^{**} \tag{15}$$

where $Y_s = \varepsilon_s v_s = \sqrt{\varepsilon_s/\mu_s}$. Finally, a linear combination of these two gives what we require

$$\hat{n} \times H = \alpha\left(\frac{1}{2}Y_1 S(\hat{n})^2 E^* - \frac{1}{2}S(\hat{n})H^*\right) + \beta\left(-\frac{1}{2}Y_2 S(\hat{n})^2 E^{**} - \frac{1}{2}S(\hat{n})H^{**}\right) \tag{16}$$

if $\alpha = 2Y_2/(Y_1 + Y_2)$ and $\beta = 2Y_1/(Y_1 + Y_2)$. A similar construction can be made for the bottom row in order to get $\hat{n} \times E$.

Using these, we come to a concise representation for

$$A(\hat{n})u = T_i \alpha_i \tilde{A}(\hat{n})^+ u^* + T_k \alpha_k \tilde{A}(\hat{n})^- u^{**} \tag{17}$$

where:

$$T_i = 2\begin{bmatrix} Y_k(Y_i + Y_k)^{-1}I & 0 \\ 0 & Z_k(Z_i + Z_k)^{-1}I \end{bmatrix} \text{ and } T_k = \begin{bmatrix} Y_i(Y_i + Y_k)^{-1}I & 0 \\ 0 & Z_i(Z_i + Z_k)^{-1}I \end{bmatrix} \tag{18}$$

and $I \in \mathbb{R}^{3 \times 3}$ is an identity matrix, and the admittance, Y, and impedance, Z, are defined as

$$Y \triangleq \sqrt{\varepsilon/\mu} \triangleq Z^{-1} . \tag{19}$$

While at PEC boundaries zero tangential electric field and the image principle can be used to derive that the linear operation of $A(\hat{n})$ on u becomes $\tilde{A}(\hat{n})u = \alpha_i T^{pc}\tilde{A}(\hat{n})^+ u^*$, where

$$T^{pc} = \begin{bmatrix} 2I & 0 \\ 0 & 0 \end{bmatrix} . \tag{20}$$

consequently, it can be shown that the scattered field formulation derived using the image principle results in:

$$\tilde{A}(\hat{n})u^s = \alpha_i T^{pc}\tilde{A}(\hat{n})^+ u^{s*} - 2\tilde{A}(\hat{n})^- G^{s*} , \tag{21}$$

where $G^{s*} = \begin{bmatrix} -E^i & 0 \end{bmatrix}^{*T}$ is the source term for the scattered field formulation.

3. Flux Integration Schemes

In order to discretize the electromagnetic problem of interest we associate with each cell a value of the generalized solution vector u_i located at the barycentre x_i of element T_i. This value is taken to represent the average of the generalized solution vector over the element T_i i.e.,

$$u_i = \frac{1}{V_i}\int_{T_i} u(x)dx = u(x_i) + O(\Delta x^2) \tag{22}$$

where V_i is the volume of element T_i, where Δx scales with the size of the element. It is apparent from (9) that integration around the boundary of an element requires knowledge of the flux (or equivalently the generalized solution vector $\boldsymbol{u}$) at both sides of the cell boundary. As we are only storing the solution at the barycentres of the elements, we require interpolation of these values to the element border in order to accurately integrate the flux. Two common techniques for flux determination at the cell boundary are so-called *upwinding* and so-called MUSCL schemes [5]. As upwinding provides only first-order accuracy, and significant dissipation, we omit it from further consideration. For brevity, details of the MUSCL scheme are omitted, however the MUSCL scheme as detailed in [5] was implemented yielding second-order accurate results as will be shown in Section 4. Further, we have applied polynomial interpolation, a method used in computational fluid dynamics to the FVTD solution to Maxwell's equations. The polynomial interpolation has been tested in CFD for up to fifth-order of accuracy. Unfortunately, in some instances (for example at some locations on the boundary of an unstructured mesh) it is not possible to maintain such high-accurate techniques for flux interpolation (see e.g. [7]). In our engine, a third-order polynomial interpolatory technique was used, and at points in the mesh where this was not possible, the MUSCL scheme was applied.

Using the above methods to approximate the flux at the boundaries i.e. $\boldsymbol{u}^*$ and $\boldsymbol{u}^{**}$ we have:

$$\frac{1}{V_i}\int_{\partial T_i} \alpha^{-1}\boldsymbol{A}(\hat{\boldsymbol{n}})\boldsymbol{u}\,ds \approx \frac{1}{V_i}\sum_{m=1}^{M_i}\left(\boldsymbol{T}_i\alpha_i\tilde{\boldsymbol{A}}(\hat{\boldsymbol{n}}_{i_m})^+\boldsymbol{u}^* + \boldsymbol{T}_{i_m}\alpha_{i_m}\tilde{\boldsymbol{A}}(\hat{\boldsymbol{n}}_{i_m})^-\boldsymbol{u}^{**}\right) \tag{23}$$

where M_i is the number of facets making up element T_i, i_m denotes the element neighbouring T_i via its mth facets and $\boldsymbol{n}_{i_m}$ denotes the outward normal to the mth facet.

Finally, for a mesh comprising of N elements we have

$$\left[\left(\frac{1}{V_1}\int_{\partial T_1}\alpha^{-1}\boldsymbol{A}(\hat{\boldsymbol{n}})\boldsymbol{u}\,ds\right)^T \left(\frac{1}{V_2}\int_{\partial T_2}\alpha^{-1}\boldsymbol{A}(\hat{\boldsymbol{n}})\boldsymbol{u}\,ds\right)^T \cdots \left(\frac{1}{V_N}\int_{\partial T_N}\alpha^{-1}\boldsymbol{A}(\hat{\boldsymbol{n}})\boldsymbol{u}\,ds\right)^T\right]^T \approx L\boldsymbol{U} \tag{24}$$

where $\boldsymbol{U} = \begin{bmatrix}\boldsymbol{u}_1^T & \boldsymbol{u}_2^T & \cdots & \boldsymbol{u}_N^T\end{bmatrix}^T$ is the vector of all unknowns. Using the result of (24) in (9) gives:

$$\partial_t \boldsymbol{U} + L\boldsymbol{U} = \boldsymbol{F} \tag{25}$$

where the time-derivative is taken element by element over $\boldsymbol{U}$ and where $\boldsymbol{F}$ is a source term where each element of $\boldsymbol{F}$ represents the right-hand-side of (9) at the ith cell. It is of importance to note that under linear flux interpolation the result of the operator L operating on $\boldsymbol{U}$ can be viewed as a matrix vector product.

Having organized the flux-integration into a matrix-vector product over the entire computational space, it remains to discretely approximate the time derivative in (25). We have considered the Forward-Euler, Predictor-Corrector, Runge-Kutta and Crank-Nicolson methods. All of these methods are explicit schemes, save Crank-Nicolson, which means that, excluding the latter, all algorithms can be computed via a matrix-vector product. In the case of the Crank-Nicolson update scheme it is necessary to solve a linear system of equations which can be accomplished using a preconditioner and iterative solver such as GMRES.

4. Numerical Results: PEC Scattering From Sphere

We present the FVTD results for scattering from a perfectly electrical conducting (PEC) sphere as an exact series solution is available. This problem was selected as a benchmark for the FVTD engine as the irregular surface of the sphere coincides with one of the primary reasons for developing finite-volume methods on irregular grids: eliminating the need for stair-stepping at arbitrarily shaped boundaries.
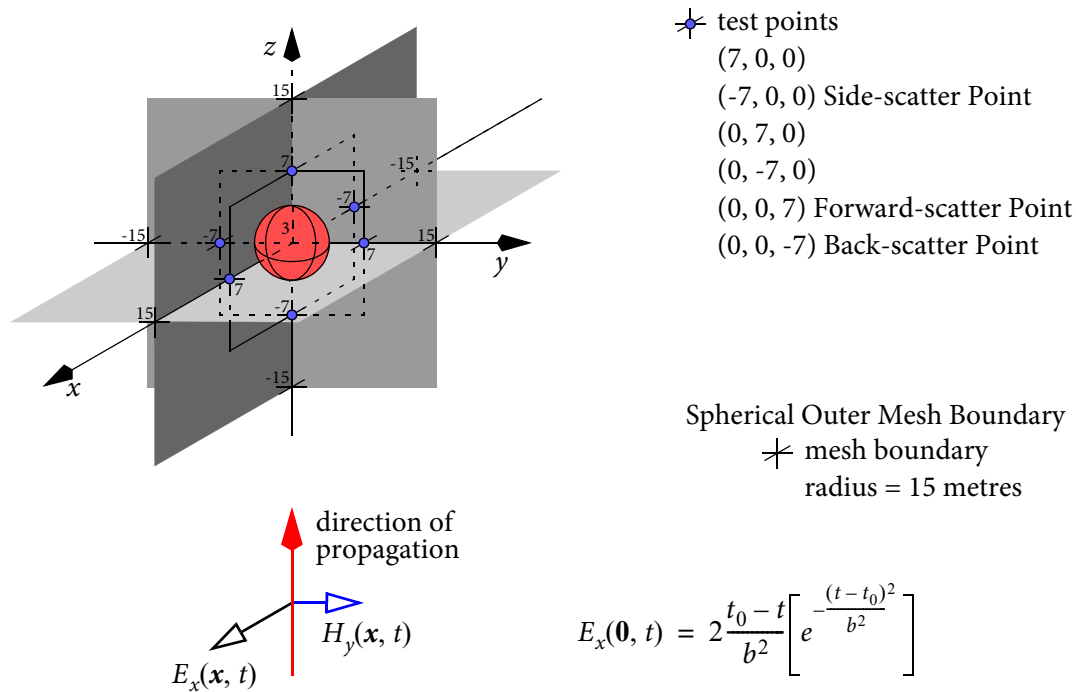
test points
(7, 0, 0)
(-7, 0, 0) Side-scatter Point
(0, 7, 0)
(0, -7, 0)
(0, 0, 7) Forward-scatter Point
(0, 0, -7) Back-scatter Point

Spherical Outer Mesh Boundary
mesh boundary
radius = 15 metres

direction of propagation

$H_y(\boldsymbol{x}, t)$

$E_x(\boldsymbol{x}, t)$

$$E_x(\boldsymbol{0}, t) \;=\; 2\frac{t_0 - t}{b^2}\left[e^{-\frac{(t - t_0)^2}{b^2}}\right]$$

Figure 1. Scattering from a PEC sphere: location of test points.

The finite-volume algorithm using the previously discussed flux- and time-integration methods was tested for a PEC sphere with a three metre radius. An x-polarized electric-field plane-wave transient pulse $g(t)$ varying as the derivative of a Gaussian was selected *i.e.*, $g(t) \;=\; -2A(t - t_0)b^{-2}\exp(-b^{-2}(t - t_0)^2)$ for $t \geq 0$. The parameters were selected as: $A = 1$, $b = 1.14 \times 10^{-8}$ s, and $t_0 = 4.0 \times 10^{-8}$ s giving a shortest free-space wavelength is about 3 metres resulting in significant energy in the resonance region of the sphere. The field quantities *i.e.*, $\boldsymbol{u}$ were computed at those points shown in Fig. 1.

FDTD results are shown in Fig. 2. In Fig. 3 we present results for the following the scattered field at back-scatter point (0, 0, -7), as well as at the side-scatter point (-7, 0, 0). For each measurement point the exact solution is presented with solutions obtained using the MUSCL and polynomial interpolation finite-volume methods for the x component of the electric field. The mesh considered coincides with average cell sizes of 0.75 m. We see that the results are in excellent agreement with the exact solution for all three electric field components.

5. Conclusions

The unstructured grid FVTD method using the MUSCL and polynomial interpolation gives excellent results as compared to the FDTD method on structured grids. This is due to the more accurate approximation of boundary conditions on curved scatterers. Currently our code is not optimized, so a proper comparison of computational resources can not be made. In future work we will compare the computational resources required to achieve the same accuracy of solution.
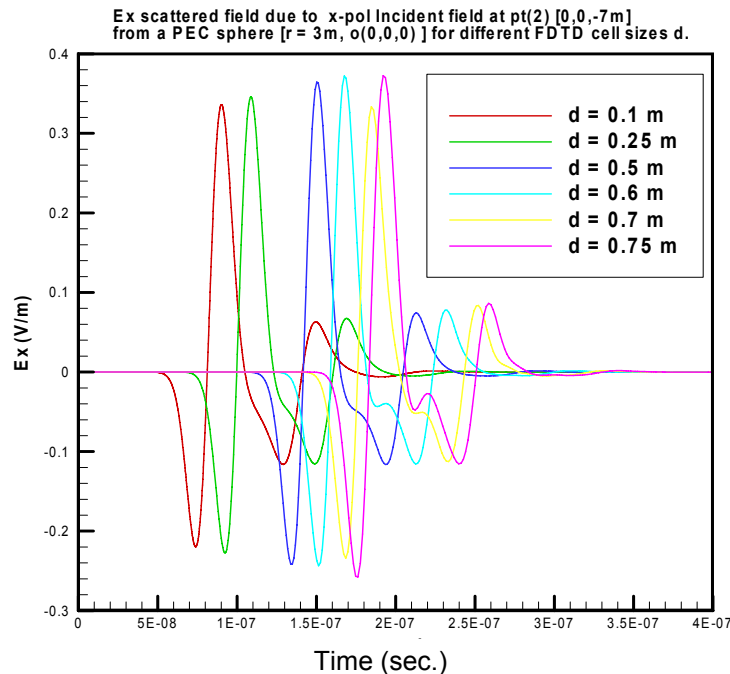
6. Acknowledgements

Figure 2. Scattering from a 3 metre PEC sphere: Back-Scattering results for FDTD depend on the mesh size

7. References

[1]   A. Taflove (editor), *Advances in Computational Electrodynamics: The Finite-Difference Time-Domain Method*, Artech House Inc, Boston, 1998.

[2]   C. Hirsch, *Numerical Computation of Internal and External Flows, Vol. I: Fundamentals of Numerical Discretization*, John Wiley & Sons Ltd., New York, 1988.

[3]   V. Shankar, A. H. Mohammadian, W. F. Hall, "A Time-Domain Finite-Volume Treatment for the Maxwell Equations," *Electromagnetics*, Vol. 10, No. 1-2, pp 127 - 145, 1990.

[4]   J. S. Shang, "Characteristic-Based Algorithms for Solving the Maxwell's Equations in the Time Domain," *IEEE Antennas and Propagation Magazine*, Vol. 37, No. 3, pp. 15-25, June 1995.

[5]   P. Bonnet, X. Ferrieres, B. L. Michielsen, P. Klotz, and J. L. Roumiguières, "Finite-Volume Time Domain Method," in *Time Domain Electromagnetics*, S. M. Rao (editor), Academic Press, San Diego, 1999.

[6]   C. Fumeaux, D. Baumann, P. Leuchtmann, and R. Vahldieck, "A Generalized Local Time-Step Scheme for Efficient FVTD Simulations in Strongly Inhomogeneous Meshes," *IEEE Trans. on MIcrowave Theory and Techniques*, Vol. 52, No. 3, pp. 1067-1076, March 2004.

[7]   C. F. Ollivier-Gooch, "Quasi-ENO Schemes for Unstructured Meshes Based on Unlimited Data-Dependent Least-Squares Reconstruction*," Journal of Computational Physics*, Vol. 133 (1), pp 6-17, 1997.
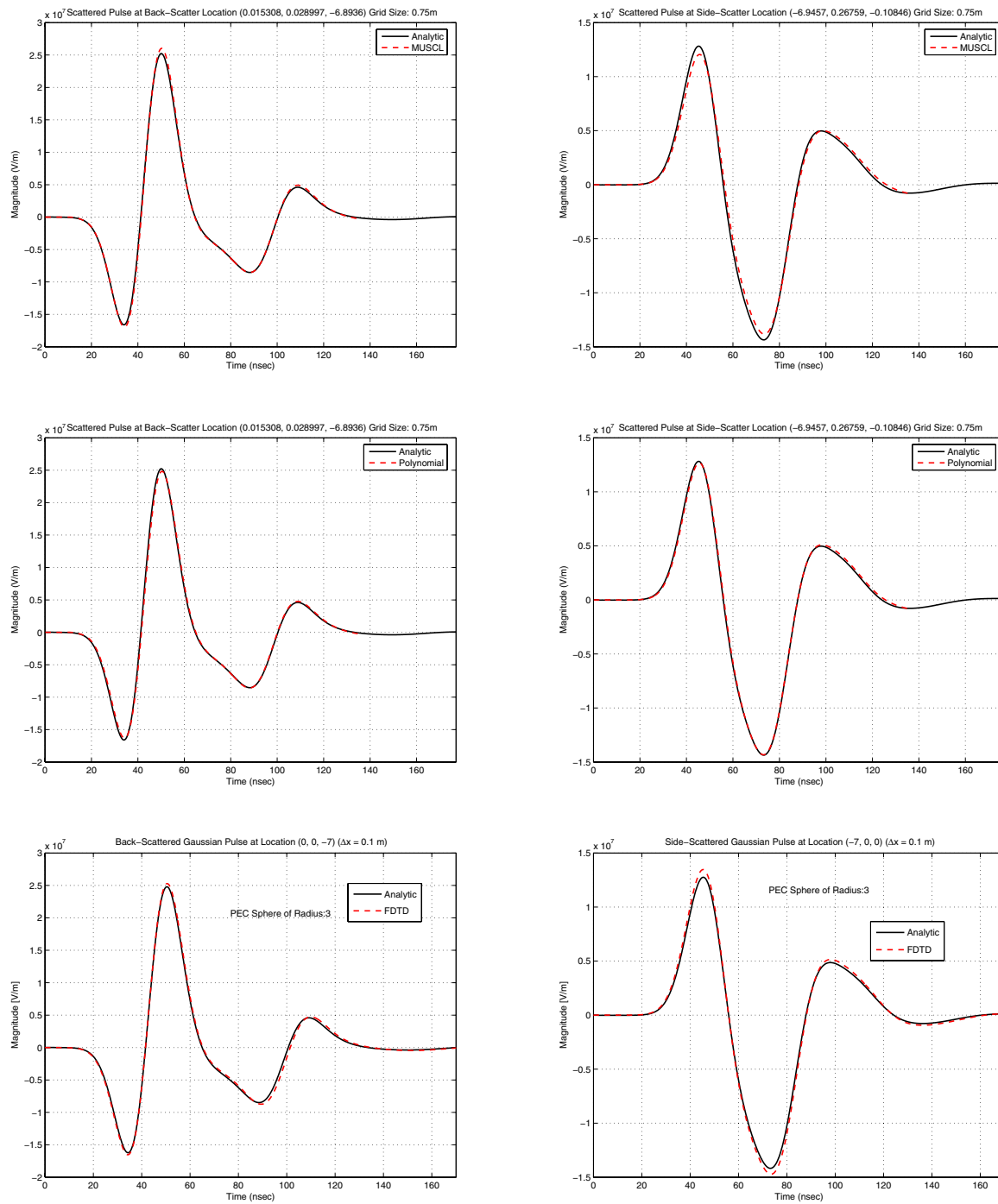
Figure 3. Scattering from a 3 metre PEC sphere: Side-Scattering (left) and Back-Scattering (right)
MUSCL (top) and Polynomial Interpolation (middle), FDTD (bottom)